Journal of Applied Electrochemistry **34**: 1029–1038, 2004.

A solid-polymer electrolyte direct methanol fuel cell with a methanol-tolerant cathode and its mathematical modelling

R.K. RAMAN[1], G. MURGIA[2] and A.K. SHUKLA[1]*
[1] *Solid State and Structural Chemistry Unit, Indian Institute of Science, Bangalore-560 012, India*
[2] *CRS4, Parco Scientifico e Tecnologico, POLARIS, Edificio 1, I - 09010 Pula, Cagliari, Italy*
*(*author for correspondence, fax: +91-80-23601310, e-mail: shukla@sscu.iisc.ernet.in)*

Received 23 February 2004; accepted in revised form 18 May 2004

Key words: solid-polymer electrolyte direct methanol fuel cells, methanol-tolerant cathode, numerical modelling

Abstract

Solid-polymer electrolyte direct methanol fuel cells (SPE-DMFCs) employing carbon-supported Pt–Fe as oxygen-reduction catalyst to mitigate the effect of methanol on cathode performance while operating with oxygen or air have been assembled. These SPE-DMFCs provided maximum power densities of 250 and 120 mW cm^{-2} at 85 °C on operating with oxygen and air, respectively. The polarization data for the SPE-DMFCs and their constituent electrodes have also been derived numerically employing a model based on phenomenological transport equations for the catalyst layer, diffusion layer and the membrane electrolyte.

List of symbols

a effective catalyst area per unit volume(cm^2 cm^{-3})
b tortuosity parameter
c_i concentration of species i (mol cm^{-3})
D_i diffusion coefficient of species i (cm^2 s^{-1})
D_{i-j} pair diffusion coefficient of gas species i and j (atm cm^2 s^{-1})
F faradaic constant (96 487 C mol^{-1})
f faradaic constant in units of RT (mV^{-1})
I operational cell current density (A cm^{-2})
i ionic current density (A cm^{-2})
$i_{0,\mathrm{ref}}$ exchange current density at reference conditions (A cm^{-2})
j transfer current per unit volume (A cm^{-3})
K_c kinetic constant for water condensation (mol s^{-1} cm^{-3} atm^{-1})
K_e kinetic constant for water evaporation (s^{-1} atm^{-1})
K_i Henry's constant for species i (atm cm^3 mol^{-1})
k_p hydraulic permeability (cm^2)
k_ϕ electrokinetic permeability (cm^2)
L^i length of region i (μ m)
N_i mass flow of species i (mol cm^{-2} s^{-1})
n number of electrons
P pressure (atm)
R gas constant (8.314 J mol^{-1} K^{-1})
R_{H_2O} water condensation/evaporation source term (mol cm^{-3} s^{-1})
S_l liquid saturation
S_i stoichiometric coefficient of species i
T temperature (K)
v water velocity (cm s^{-1})
x_i molar fraction of species i
z fixed-site charge

Greek symbols

α_a anodic transfer coefficient
α_c cathodic transfer coefficient
γ kinetic factor
ΔP decay parameter for electrode flooding (atm)
ε Porosity
η interface overpotential (mV)
κ ionic conductivity (Ω^{-1} cm^{-1})
μ water viscosity (kg m^{-1} s^{-1})
ϕ_l electric potential of liquid phase (mV)
ϕ_s electric potential of solid phase (mV)
ρ water density (mol cm^{-3})
σ electronic conductivity (Ω^{-1} cm^{-1})

Subscripts and superscripts

a anode
c cathode
eff effective value
f fixed charge
g gas phase
l liquid phase
ref reference conditions
s solid phase
t total (liquid + gas)
sat saturated vapour
w water

1. Introduction

In a direct-methanol fuel cell, aqueous methanol is directly oxidized at the anode to carbon-dioxide and

protons, which travel through a proton conducting membrane electrolyte, usually Nafion®, towards the cathode to facilitate reduction of oxygen to water. The respective electrochemical reactions in a solid-polymer electrolyte direct methanol fuel cell (SPE-DMFC) at the anode and cathode are,

$$CH_3OH + H_2O \rightarrow CO_2 + 6H^+ + 6e^- \quad (E_a^\circ = 0.02\,V \text{ vs SHE}) \tag{1}$$

and

$$\frac{3}{2}O_2 + 6H^+ + 6e^- \rightarrow 3H_2O \quad (E_c^\circ = 1.23\,V \text{ vs SHE}) \tag{2}$$

Accordingly, the net cell reaction in a SPE-DMFC is

$$CH_3OH + \frac{3}{2}O_2 \rightarrow CO_2 + 2H_2O \quad (E_{Cell}^\circ = 1.21\,V) \tag{3}$$

However, owing to methanol permeability across the membrane, the performance of the cathode, which usually comprises a carbon-supported platinum catalyst, is affected substantially [1–4]. Therefore, there is a need to develop SPE-DMFCs with a methanol-tolerant cathode. This has been achieved with the use of ruthenium chalcogenide catalysts, namely RuS and RuSe [5–13]. However, the power densities achieved with SPE-DMFCs employing such cathodes are rather limited [14].

In this communication, we report a SPE-DMFC comprising a carbon-supported Pt–Fe alloy-catalyst cathode, which exhibits substantial tolerance to methanol. Such a SPE-DMFC could provide power densities as high as 250 and 120 mW cm^{-2} at 85 °C while operating with oxygen and air cathodes, respectively. A one-dimensional, two phase, multicomponent steady-state mathematical model for the SPE-DMFCs based on phenomenological transport equations for the catalyst layer, diffusion layer and polymeric electrolyte membrane is also presented. In particular, the simulated performance data for an oxygen-fed cathode with the non-selective catalyst and DMFC polarization data with an air-fed cathode with the selective catalyst fit closely with the experiments.

2. Experimental details

2.1. *Preparation of Pt/C and Pt–Fe/C catalysts*

The Sulfito-complex route [2,15–17] was adopted to prepare 20 wt % platinized carbon (Pt/C). To prepare carbon-supported Pt–Fe (1:1 atomic ratio) alloy catalyst (Pt–Fe/C), 500 mg of 20 wt % Pt/C along with 207 mg of ferric nitrate [$(Fe(NO_3)_3 \cdot 9H_2O$] was dispersed in a 1:1 mixture of 10 ml of isopropyl alcohol and millipore water followed by ultrasonication for about 0.5 h [18]. When the pH was adjusted to 7 using 0.1 M solution of hydrazine, formation of colloidal ferric hydroxide occured followed by deposition of ferric hydroxide on Vulcan-XC 72 R carbon and the slurry thus obtained was dried with constant stirring. The resultant mass was transferred into an alumina boat and alloyed by heating at 750 °C for 1 h under flowing hydrogen followed by annealing for 12–15 h.

To test the chemical stability of Pt–Fe/C catalyst, 40 mg of 20 wt % Pt–Fe/C was suspended in 20 ml of 0.5 M H_2SO_4 solution while maintaining the temperature of the slurry at 85 °C with constant stirring for 16 h. Samples were taken intermittently at various times. 0.5 M H_2SO_4 was chosen because Nafion® membrane has an acid capacity (or molar equivalent weight) of 0.89 meq g^{-1} (i.e., $\sim$1 eq kg^{-1}), which is equivalent to 0.5 M H_2SO_4 [19]. The slurries were filtered and the filtrates were diluted appropriately to examine the presence of iron using a pre-calibrated VIDEO-11E Thermo Jarrell Ash atomic absorption spectrophotometer.

Both 20 wt % Pt/C and 20 wt % Pt–Fe/C catalysts were characterized by recording their powder X-ray diffraction (XRD) patterns on a Siemens D-5005 X-ray diffractometer using CuK_α-radiation. The catalysts were also subjected to energy dispersive analysis by X-rays (EDAX) employing a Jeol JSM-840A scanning electron microscope to determine the composition of their constituent elements.

2.2. *Assembly of SPE-DMFCs with Pt/C and Pt–Fe/C cathodes, and their electrochemical characterization*

Membrane electrode assemblies (MEAs) were obtained by sandwiching the pretreated Nafion®-117 polymer electrolyte membrane between the anode and cathode [20]. Both the anode and cathode consist of a backing layer, a gas-diffusion layer and a reaction layer. A Teflonized (20 wt % PTFE) carbon paper (Toray TGP-H-090) of 0.28 mm thickness was employed as the backing layer in these electrodes. To prepare the gas diffusion layer, Vulcan XC-72R carbon was suspended in water and agitated in an ultrasonic water bath. To this, 13 wt % PTFE (Fluon GP-2) suspension was added with continuous agitation. The required amount of cyclohexane was then added to it dropwise. The resultant slurry was spread onto a Teflonized carbon paper and dried in an air oven at 80 °C for 2 h. To prepare the reaction layer, the catalyst ink was obtained by suspending the catalyst (20 wt % Pt/C or 20 wt % Pt–Fe/C on the cathode and 60 wt % Pt–Ru/C on the anode) in isopropyl alcohol (100 mg catalyst in 10 ml of isopropyl alcohol). Subsequently, the mixture was agitated in an ultrasonic water bath, and 10 wt % of Nafion® solution was added to it with continuing agitation for 1h. The ink thus obtained was coated onto the gas-diffusion layer of the electrode. The anode contained 60 wt % Pt–Ru (1:1 atomic ratio) carbon-supported catalyst prepared in-house with platinum

loading of 1 mg cm^{-2}, which was kept identical in all the MEAs. The platinum content at the cathode in all the MEAs was maintained at 1 mg cm^{-2}. A Nafion loading of 0.25 mg cm^{-2} was applied to the surface of each electrode. The membrane electrode assembly was obtained by hot pressing the cathode and anode on either side of a pre-treated Nafion®-117 membrane at 60 kg cm^{-2} at 125 °C for 3 min.

Liquid-feed SPE-DMFCs were assembled with various MEAs. The anode and cathode of the MEAs were contacted on their rear with gas/fluid flow field plates machined from high-density graphite blocks in which channels were machined to achieve minimum mass-polarization in the SPE-DMFCs. The ridges between the channels make electrical contact with the rear of the electrode and conduct the current to the external circuit. The channels supply methanol to the anode and oxygen or air to the cathode. Electrical heaters were placed behind each of the graphite blocks to heat the cell to the desired temperature. A 2 M methanol solution was pumped to the anode chamber through a peristaltic pump and the unreacted solution was collected in the reservoir. Oxygen or air gas at 2 bar pressure was introduced into the cathode chamber. The graphite blocks were also provided with electrical contacts and tiny holes to accommodate thermocouples. After installing the single cell in the test station, performance evaluation studies were initiated. To humidify the Nafion® membrane, humidified H_2 and O_2 were passed at anode and cathode, respectively, while maintaining the cell temperature at 60 °C and loading it at a current density of about 100 mA cm^{-2}.

To characterize methanol poisoning effect on Pt/C and Pt–Fe/C catalysts towards oxygen reduction reaction, cyclic voltammogram on these catalyst electrodes were also obtained using a three-electrode cell configuration in 0.5 M H_2SO_4 electrolyte with and without methanol at 60 °C employing an AutoLab PGSTAT-30 electrochemical system. The electrochemical cell comprised the working electrode, which was Pt/C or Pt–Fe/C electrode, a counter electrode made of Pt–Pd mesh, and a SHE as reference electrode. Working electrode was constructed from a high-density graphite rod on one end of which Pt/C or Pt–Fe/C catalyst, each with a Pt loading of 0.5 mg cm^{-2}, was coated using catalyst ink with 10 wt % Nafion® supplied as 5 wt % Nafion solution from Aldrich. Cyclic voltammograms were recorded in the potential range 0.0 V and 1.3 V vs SHE at a scan rate of 10 mV s^{-1}.

Galvanostatic-polarization data for oxygen–reduction reaction on Pt/C and Pt–Fe/C cathodes were obtained at 85 °C by passing oxygen/air at 2 bar pressure and the hydrogen at anode to use it as a standard hydrogen electrode (SHE). On polarizing the DMFC anode, hydrogen was evolved at the cathode according to the reaction: 6 H^+ + 6 e^- → 3 H_2, which served as a SHE to obtain anode polarization data. The cell polarization data at 85 °C were obtained by circulating 2 M aqueous methanol at the anode and 2 bar oxygen at the cathode.

3. Mathematical model for the SPE-DMFCs

A one dimensional, steady-state, multicomponent, two phase mathematical model [21, 22] was applied for the mechanistic interpretation of the experimental performance curves. The model employs mass conservation for the chemical species, and charge conservation both for protons and electrons, and is centered on three important requisites: (a) an appropriate description of transport and reaction mechanism determining the performance of the SPE-DMFC and PEFC, (b) an analytical treatment of principal nonlinear terms arising from kinetic equations, which gives an efficient and fast numerical solution of the mathematical model, and (c) the inclusion of two-phase phenomena such as water and gas flooding, and water condensation–evaporation transition. The model considers the fuel cell to comprise five regions, namely anode diffuser, anode catalyst, membrane, cathode catalyst, and cathode diffuser. The independent variables of the model are the electrical potential of the solid (ϕ_s) and liquid (ϕ_l) phases, the hydraulic pressure (P), concentrations of methanol (c_{CH_3OH}), carbon dioxide (c_{CO_2}), and oxygen (c_{O_2}) in the liquid phase, and oxygen and water vapour molar fractions (x_{O_2}, x_{H_2O}) in the gas phase. The molar fraction of the nitrogen (x_{N_2}) and the gas porosity (ε_g) are dependent variables in the model. While modeling the PEFC cell polarization data, methanol and carbon dioxide concentrations are replaced by the hydrogen mole fraction in the gas phase (x_{H_2}) and concentration in the liquid phase (c_{H_2}). Any spatial variation in the variables is governed by the respective phenomenological expressions, which relate the flux of any physical quantity to its generating force. The main assumptions in the model are: (a) steady-state operation of the cell, (b) constant temperature (isothermal) operation of the cell, (c) zero differential gas pressure in the porous medium, (d) fully-hydrated electrolyte membrane, and (e) liquid-phase transport of reactants at the anode for the SPE-DMFC cells. The systems of coupled differential equations employed in the model are given in Table 1.

The Butler–Volmer (BV) equation employed in the model for the hydrogen reaction is,

$$\nabla \cdot i_a = a i^a_{0,\mathrm{ref}} \left(\frac{c^a_{H_2}}{c^{\mathrm{ref}}_{H_2}} \right)^{\gamma_a} \left[e^{\alpha_a f \eta_a} - e^{-(1-\alpha_a) f \eta_a} \right] \tag{4}$$

When methanol oxidation and oxygen reaction are accounted, the Butler–Volmer equation takes the Tafel form for the irreversible polarization regimes as described below:

$$\nabla \cdot i_a = a i^a_{0,\mathrm{ref}} \left(\frac{C^a_{CH_3OH}}{C^{\mathrm{ref}}_{CH_3OH}} \right)^{\gamma_a} \left[e^{\alpha_a f \eta_a} \right] \tag{5}$$

where $f = F/RT$ and $\eta_a = \phi_{s,a} - \phi_{l,a}$, and

Table 1. Systems of coupled differential equations employed in the model

Equations	Phemnomenological equation
$\nabla \cdot (D_j \varepsilon^{b} \nabla c_j - c_j v) = 0$	Nernst–Planck
$= y_j$	
$\nabla x_i = \sum_{j=1}^{n} \frac{RT}{PD_{i-j}\varepsilon^{b}}(x_i N_j - x_j N_i)$	Stefan–Maxwell
where $j = O_2, N_2, H_2O$	
$\nabla \cdot (\sigma \nabla \phi_s) = 0$	
$= j^{a}$	Ohm's law
$= j^{c}$	
$\nabla \cdot (\kappa \varepsilon^{b} \nabla \phi_l + F c_f v) = 0$	
$= j^{a} - (F c_f/\rho) y_{H_2O}$	Nernst–Planck
$= j^{c} - (F c_f/\rho) y_{H_2O}$	
$\nabla \cdot (-(k_p/\mu) S^{b} \nabla P) = 0$	
$\nabla \cdot (a \nabla \phi_l - (k_p/\mu) \nabla P) = 0$	Darcy Modified Schlögl
$= -(1/\rho) y_{H_2O}$	
$= -(1/\rho) y_{H_2O}$	

In the above Table: $a = \frac{k_\phi}{\mu} z_f c_f F$ and $y_i = \frac{s_i^\beta}{n^\beta F} j^\beta$, where $\beta = a, c$. In the case of analytical integration of Butler–Volmer equations: $y_i = j^{a} = j^{c} = 0$ in A_R, C_R and with i = CH_3OH, CO_2, O_2, H_2O

$$\nabla \cdot i_c = a i_{0,\mathrm{ref}}^{c} \left(\frac{c_{O_2}^{c}}{c_{O_2}^{\mathrm{ref}}} \right)^{\gamma_c} \left[-e^{-\alpha_c f \eta_c} \right] \tag{6}$$

where $\eta_c = \phi_{s,c} - \phi_{l,c}$.

In the set of transport equations, the BV equation appears as a mass and charge production/consumption term (source term) as shown above.

Gas and water flooding at the anode and cathode diffuser, respectively, is accounted by means of a simple gaussian term as follows:

$$\begin{cases} \varepsilon_g = \varepsilon_{g,0} e^{-(P_c/\Delta P_g)^2} & \text{when } P_g \leqslant P_l \\ \varepsilon_g = \varepsilon_t - \varepsilon_{l,0} e^{-(P_c/\Delta P_l)^2} & \text{when } P_g > P_l \end{cases} \tag{7}$$

where $\varepsilon_t (= \varepsilon_g + \varepsilon_l = (V_g + V_l)/V_t)$ is the total porosity of the fluid phases, $\varepsilon_l (= V_l/V_t)$ is the porosity of the liquid phase, and ΔP_g and ΔP_l are the decay terms of the gaussian function and represent water and gas flooding in the diffuser layer, respectively. The subscript '0' in Equation 7 refers to values of the porosity parameters at the diffuser layer/reactant delivery structure interface. $(V_g + V_l)$ is the fluid phase volume, where V_g is the gas phase volume and V_l is the liquid phase volume and V_t is the total volume, which is obtained by adding the solid phase volume V_s to the fluid phase volume, that is $V_t = V_g + V_l + V_s$.

In the model, the mass exchange among liquid and gaseous phases due to water evaporation–condensation is treated following the approach adopted by Natarajan and Nguyen [23] as

$$R_{H_2O} = K_e \rho \varepsilon_l (P_{H_2O}^{sat} - P_g x_{H_2O}) Sw - K_c \varepsilon_g x_{H_2O} (P_g x_{H_2O} - P_{H_2O}^{sat}) \times (1 - Sw) \tag{8}$$

where Sw is a switch function and is equal to 1 for $(P_{H_2O}^{sat} - P_g x_{H_2O}) > 0$ and is 0 when $(P_{H_2O}^{sat} - P_g x_{H_2O}) < 0$.

R_{H_2O} is a kinetic mass-transfer term at the liquid–gas interface and is expressed by

$$\nabla \cdot N_{H_2O} = R_{H_2O} \tag{9}$$

and

$$\nabla \cdot v = -\frac{R_{H_2O}}{\rho} \tag{10}$$

The model does not include the mass exchange among liquid and gaseous phases for the other chemical species in the diffusive region.

Most of the equations of the model are mechanistic and their parameters are physico-chemical bulk transport properties of materials such as the hydraulic and electrokinetic permeability, diffusion coefficient of chemical species in the different phases of the MEA, electronic and ionic conductivities of the materials. Furthermore, the model employs a number of geometrical parameters such as the thickness of each cell layer. The above parameters, but for the electronic conductivity, were not fitted to the experiments and their values, reported in Table 2, were taken from the literature. The electronic conductivity was fitted to the experimental cell since its value reflects the electrical contact resistance rather than the bulk behaviour of the conducting material. The contact resistance depends on the cell fabrication technique and it may vary from cell to cell. The model contains a few empirical equations accounting for water condensation–evaporation, water flooding and the electrode kinetics. In the literature, model parameters such as the kinetic terms, namely α_c, α_a, γ in Equations 4–6, the water flooding ΔP_g in Equation 7, and the water condensation–evaporation, namely K_c and K_e in Equation 8, have already been reported from extensive comparison with experimental data [21, 22] and, hence, these are also not fitted to the experiments. The only parameters adjusted to describe the experimental results are the preexponential kinetic parameter $ai_{0,\mathrm{ref}}$, the gas porosity of the cathode catalyst layer ε_g^c, the gas porosity at the diffuser layer/reactant delivery structure interface $\varepsilon_{g,0}$, besides the above mentioned electronic conductivity (σ). The fitting protocol was developed according to the following scheme. Both the anode kinetic parameter $ai_{0,\mathrm{ref}}$, and the electronic conductivity (σ) for the anode diffuser were obtained by a comparison with the anode polarization data and $\varepsilon_{g,0}$ for the cathode diffuser was obtained by comparison with the H_2/Air cell polarization data. The physico-chemical and geometrical parameters, these parameters were also not varied in the model with the operative conditions during the simulation of the cell

Table 2. Physicochemical and kinetic parameters employed in the numerical modelling

			References
Membrane parameters			
Ionic conductivity	κ	0.158 Ω^{-1} cm^{-1}	[29]
CH_3OH Diffusivity	D_{CH_3OH}	8.2×10^{-6} cm^2 s^{-1}	[30]
O_2 Diffusivity	D_{O_2}	1.36×10^{-6} cm^2 s^{-1}	[31]
Fixed charge concentration	c_f	1.2×10^{-3} mol cm^{-3}	[32]
O_2 Henry's constant	K_{O_2}	2.10×10^5 atm cm^3 mol^{-1}	[31]
Hydraulic permeability	k_p	1.8×10^{-14} cm^2	[32]
Electrokinetic permeability	k_ϕ	7.18×10^{-16} cm^2	[32]
Water viscosity	μ	3.5×10^{-4} kg m^{-1} s^{-1}	[33]
Water density	ρ	0.054 mol cm^{-3}	[33]
Electrode parameters			
Electronic conductivity	κ	0.50 Ω^{-1} cm^{-1}	this work
CH_3OH Diffusivity (in water)	D_{CH_3OH}	9.7×10^{-5}cm^2 s^{-1}	[34]
CO_2 Diffusivity (in water)	D_{CO_2}	1.0×10^{-4} cm^2 s^{-1}	–
O_2–N_2 Pressure diffusivity	$D_{O_2-N_2}$	0.287 atm cm^2 s^{-1}	[32]
O_2–H_2O Pressure diffusivity	$D_{O_2-H_2O}$	0.386 atm cm^2 s^{-1}	[32]
H_2O–N_2 Pressure diffusivity	$D_{H_2O-N_2}$	0.404 atm cm^2 s^{-1}	[32]
Membrane fraction in catalyst layer	ε_m	0.4	[32]
Membrane fraction in membrane region	ε_m	1.0	[21]
Diffuser layer total porosity	ε_t	0.8	[21]
Hydraulic permeability	k_P	4.55×10^{-14}cm^2	
Kinetic parameters			
Preexponential parameter in BV equations	$ai_{0,ref}$	(Table 2)	
Cathodic transfer coefficient	α_c	1.2 oxygen reduction	[22]
Anodic transfer coefficient	α_a	1.0 methanol oxidation 0.5 hydrogen oxidation	[21, 22]
O_2 Concentration parameter	γ_{O_2}	1.0	[22]
CH_3OH Concentration parameter	γ_{CH_3OH}	0.5	[21]
H_2 Concentration parameter	γ_{H_2}	0.25	[32]
O_2 Reference concentration	$c_{O_2,ref}$	4.71×10^{-6} mol cm^{-3}	
CH_3OH Reference concentration	$c_{CH_3OH,ref}$	1.0×10^{-3} mol cm^{-3}	
H_2 Reference concentration	$c_{H_2,ref}$	5.64×10^{-5} mol cm^{-3}	
CH_3OH Stoichiometric coefficient	s_{CH_3OH}	1	
CO_2 Stoichiometric coefficient	s_{CO_2}	−1	
H_2O Stoichiometric coefficient	s_{H_2O}	1 anode 3 cathode	
O_2 Stoichiometric coefficient	s_{O_2}	−3/2	
H_2 Stoichiometric coefficient	s_{H_2}	0.5	
Number of electrons	n	6 (methanol ox) 1 (hydrogen ox) 4 (oxygen red)	
Cathode catalyst layer gas porosity	ε_g^c	0.0057 H_2 feed 0.0034 CH_3OH feed	this work
Flooding parameters			
Decay parameter for water flooding	ΔP_g ΔP_l	0.38 atm cathode 1.10 atm anode	[21]
Diffuser layer gas porosity	$\varepsilon_{g,0}$	0.51 anode 0.15 cathode	this work
Other empirical parameters			
Kinetic constant for water condensation	K_c	5.0×10^{-5} mol s^{-1} cm^{-3} atm^{-1}	[21]
Kinetic constant for water evaporation	K_e	5.0×10^{-3} s^{-1} atm^{-1}	[21]
Tortuosity parameter	b	1.5	[21]
Physical and operative parameters			
Membrane thickness	–	200 μm	
Diffusive region thickness	–	260 μm	
Catalyst layer thickness	–	10 μm	
Geometrical electrode area	A	25 cm^2	
Cell temperature	T	85 °C	
Methanol feed concentration	$c_{CH_3OH}^{AF}$	2.0 M	
Anode inlet pressure	P_a^{in}	1 atm	
Cathode inlet pressure	P_c^{in}	3 atm	
Nitrogen–Oxygen mole ratio (air feed)	–	0.79/0.21	
Anode feed flow rate (liquid)	–	15 cm^3 min^{-1}	
Cathode feed flow rate (gas)	–	1000 cm^3 min^{-1}	
Humidity content in cathodic gas feed	–	0	

Table 3. $ai_{0,ref}$ Preexponential parameter in BV equations expressed in A cm^{-3}

	H_2–O_2	H_2–Air	CH_3OH–O_2	CH_3OH–Air
Anode	5.6×10^5	5.6×10^5	4.4×10^{-2}	4.4×10^{-2}
Cathode Pt/C	7.0×10^{-5}	7.0×10^{-6}	2.0×10^{-6}	1.5×10^{-5}
Cathode Pt–Fe/C	8.0×10^{-6}	7.0×10^{-7}	8.0×10^{-6}	8.0×10^{-6}

performance. Different values of the gas porosity of the cathode catalyst layer ε_g^c were used for the cells fed with hydrogen and methanol, in order to account for the difference in the electrolyte hydration conditions for gas and liquid feed at the anode. The cathode kinetic parameter ($ai_{0,ref}$) for both the catalysts Pt and Pt–Fe were obtained by comparing H_2/O_2 and H_2/Air polarization data. Its value was subsequently adjusted for methanol feed to reflect the decrease in catalyst active area per unit volume (a) due to methanol adsorption on the catalyst surface. All model parameters are listed in Tables 2 and 3.

4. Results and discussion

The nominal composition of the Pt–Fe/C alloy catalyst was 20 wt % Pt–Fe (1:1 atomic ratio) while EDAX composition of the constituent elements in this alloy catalyst indicated 46 Fe:54 Pt in atomic % ratio. Powder XRD patterns of 20 wt % Pt/C, 20 wt % Pt–Fe/C, and Pt–Fe/C catalyst exposed to 0.5 M aqueous H_2SO_4 for 16 h are shown in Figure 1(a) – (c), respectively. The diffraction peak at $2\theta \approx 25°$ in all the XRD patterns is due to the (002) plane of the hexagonal structure of Vulcan XC-72R carbon. While the XRD pattern for Pt/C catalyst indicates a face-centred cubic phase [24], the XRD pattern for Pt–Fe/C catalyst resembles an ordered face centered tetragonal phase [25]. It has been documented that annealing of Pt–Fe catalysts results in conversion from a disordered face centred cubic phase to chemically ordered face centred tetragonal phase [25]. The values of lattice parameters for Pt/C and Pt–Fe/C catalysts as obtained from their XRD patterns are $a = 3.923$ Å and $a = 3.852$ Å, $c = 3.713$ Å, respectively. Using the Williamson–Hall plot [26], the particle size in the Pt/C and Pt–Fe/C catalysts are found to be 3 and 11 nm, respectively. There were little differences in the XRD patterns of the Pt–Fe/C alloy sample prior and after exposing it to 0.5 M aqueous H_2SO_4. As observed from atomic absorption spectroscopy, there was only 0.6 ppm leaching of Fe from the alloy sample only during the first 4 h. However, there was no leaching subsequently suggesting that the Pt–Fe probably had some free iron present in the alloy sample, which was not detectable from XRD patterns.

The cyclic voltammograms obtained to characterize the methanol poisoning effect on Pt/C, and Pt–Fe/C catalysts towards oxygen reduction reaction in aqueous sulfuric acid both with (Figure 2(b)) and without (Figure 2(a)) methanol are shown in Figure 2. Pt–Fe/C appears to be a potential methanol-tolerant oxygen reduction catalyst. The higher oxygen-reduction activity of the Pt–Fe/C catalyst in the presence of methanol appears to be primarily due to (a) the higher proportion of active platinum sites in relation to Pt/C, and (b) a completely

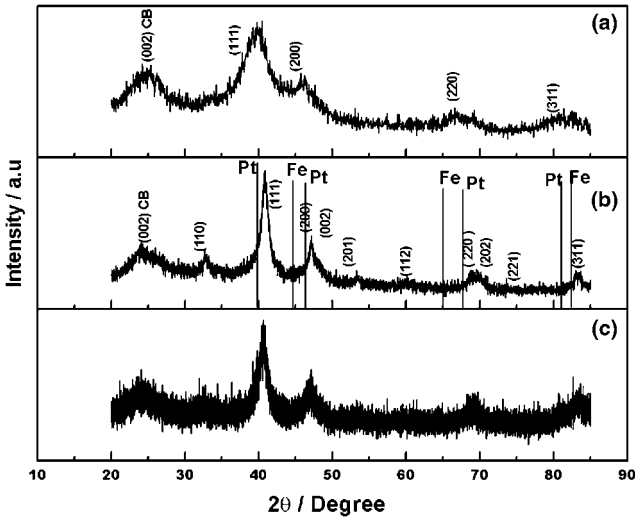

Fig. 1. X-ray power diffraction patterns for (a) as-prepared Pt/C catalyst, (b) as-prepared Pt–Fe/C catalyst, and (c) Pt–Fe/C catalyst exposed to 0.5 M aqueous H_2SO_4 for 16 h at 85 °C.

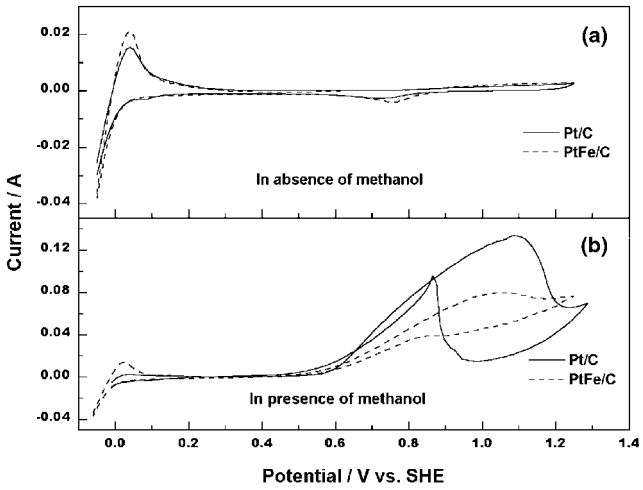

Fig. 2. Cyclic voltammograms for Pt/C and Pt–Fe/C with and without methanol in 0.5 M aqueous H_2SO_4 (sweep rate = 10 mV s^{-1}).

different nearest neighbour environment in the Pt–Fe/C catalyst where, unlike the Pt/C catalyst, the nearest neighbour sites are occupied by Fe, which helps to scavenge impurities from the neighbouring active platinum sites [27]. The above conjuctures were arrived at from X-ray photoelectron and X-ray absorption spectroscopic studies. Also, Pt–Fe/C was reported to be a potential CO-oxidation catalyst [28].

The cathode polarization curves for oxygen reduction using Pt/C, and Pt–Fe/C catalysts obtained by oxidizing hydrogen at the anode, which also acts as the reference electrode, are shown in Figure 3(a). These data show superior performance for the Pt/C cathode. But while passing the methanol at the anode, a lower cell performance was found for the cell employing Pt/C catalyst in relation to Pt–Fe/C cathode as shown in Figure 3(b). This clearly reflects the poisoning of the Pt/C cathode due to methanol cross-over from anode to the cathode since the anode performance for both the cells was nearly identical. A similar study was conducted with the air cathode, and the data are presented in Figure 4(a) and (b).

Mathematical modelling has been used both for a mechanistic interpretation of the experimental polarization data and to extract information not easily accessible from experiments. As a first application, the model was used to estimate anode polarization data when the cathode is fed with pressurized gasses. Figure 5 shows simulated anode polarization data for the DMFC with its cathode pressurized at 3 atm oxygen (or air) oxidant

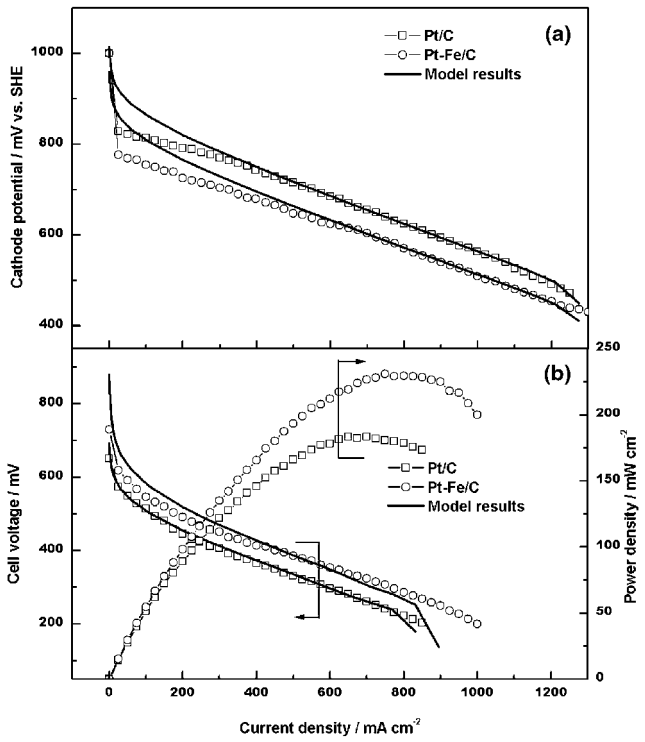

Fig. 3. (a) Cathode polarization curves obtained at 85 °C for oxygen reduction using oxygen-fed Pt/C or Pt–Fe/C cathode, and (b) SPE-DMFC polarization data obtained at 85 °C with Pt–Ru/C anode and Pt/C, or Pt–Fe/C cathode. Model results are shown in full lines.

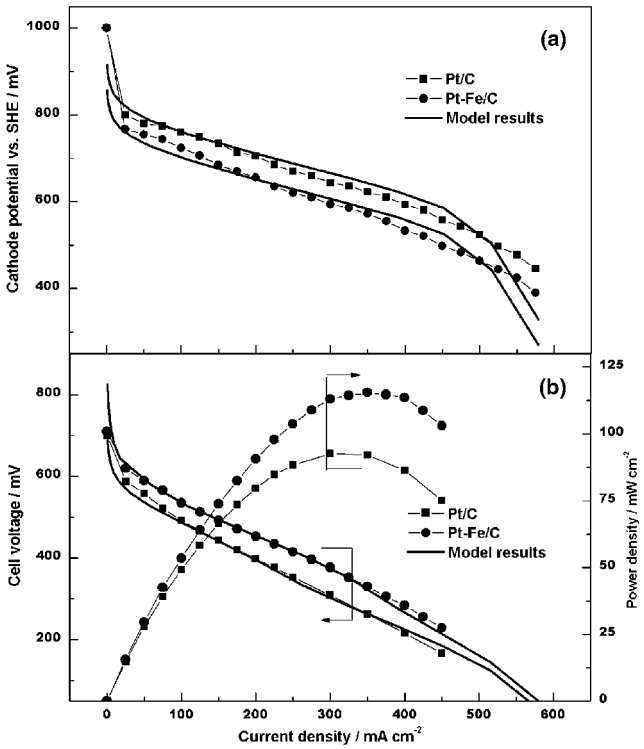

Fig. 4. (a) Cathode polarization curves obtained at 85 °C for oxygen reduction using air-fed Pt/C or Pt–Fe/C cathode, and (b) SPE-DMFC polarization data obtained at 85 °C with Pt–Ru/C anode and Pt/C, or Pt–Fe/C cathode. Model results are shown in full lines.

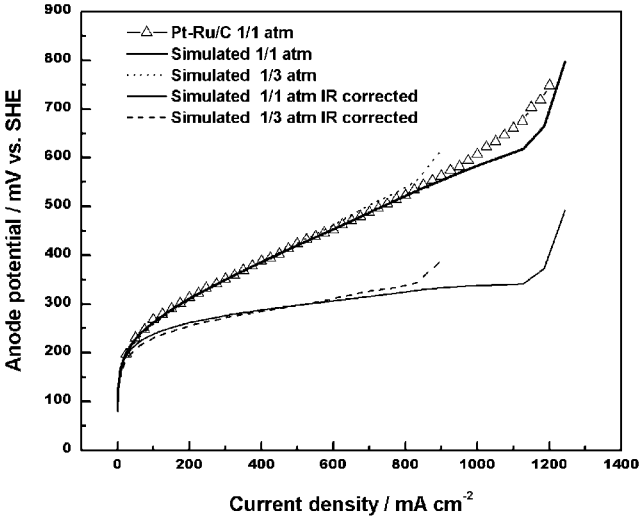

Fig. 5. Experimental and simulated anode polarization curve obtained at 85 °C with Pt–Ru/C anode.

and compares it with the experimentally obtained anode polarization curve. Increasing cathode pressure to 3 atm facilitates the convective component for water motion within the cell from cathode to anode while resisting methanol transport from anode to cathode. In this study, this would imply to a shift of the anode limiting current from around 1300 to 900 mA cm^{-2}. The simulation results agree well with the measured limiting

current for the DMFCs fed with pure oxygen (Figure 3(b)). This verifies that performance of the experimental DMFCs are anode limited when the cells are fed with pressurized oxygen. At the current densities far from limiting value, the anode polarization exhibits very little effect due to pressurized cathode.

The modelling analysis of the anode performance has also been employed to separate the anode interface overpotential, namely the activation and mass transfer overpotential from the ohmic overpotential. The analysis of the low current density range up to 200 mA cm^{-2} in the ohmic-corrected curves in Figure 5 reveals a kinetic activation polarization of about 250 mV. From 200 to 800 mA cm^{-2}, the logarithmic tail of the kinetic activation and the rising mass transfer component cause a further loss of 50 mV, with an abrupt increase while approaching the limiting current.

The knowledge of anode and ohmic contributions to cell polarization is important for evaluating the cathode polarization and, consequently, the performance behaviour of both Pt and Pt–Fe cathode catalysts. In this respect, the calculation of the methanol cross-over flux at the experimental operative conditions and the evaluation of its effect on the cathode polarization is of relevance and will be referred to as cross-over overpotential. Model results of methanol cross-over flux are plotted in Figure 6(a). From the data, methanol cross-over current density is about 150 mA cm^{-2} at low load current density intervals. This value reduces with increasing current densities due to the increase in anodic consumption of methanol, until it approaches zero at the anode limiting current density. Methanol can affect cathode polarization in two ways: namely, (i) the reduction of the active catalyst area due to its adsorption, and (ii) the development of a parasitic current due to its electrochemical oxidation. Effects of the parasitic current on cathode potential have been evaluated as the difference between the cathode overpotential computed by assuming selective and non-selective behaviours of the catalysts, and results are shown in Figure 6(b) both for oxygen and air feeds. Cross-over overpotential depends strongly both on load current densities and on the oxygen concentration at the cathode catalyst layer. In the low current density range between (0–150 mA cm^{-2}), the cross-over overpotential reflects the logarithmic behaviour of oxygen kinetic activation. In this range, the parasitic current, rather than the load current density, induces the electrode polarization due to kinetic activation. In the medium load current density range, the oxygen concentration plays an important role on the magnitude of cross-over overpotential. When the oxygen concentration is high, as in the case of pressurized oxygen feed, the cross-over overpotential decays monotonically following a reduction in methanol cross-over flux with increasing load current density. When the cathode is fed with air, the behaviour of the cross-over overpotential is more complex, and after the activation decay at low current densities, the cross-over overpotential increases to a maximum of 75 mV at a load current density of about 300 mA cm^{-2}. The presence of a maximum in the cross-over overpotential may be further explained on the basis of cathode permeation of methanol. The presence of methanol at the cathode catalyst layer yields a parasitic current which consumes oxygen with no production of electric work. The parasitic current induces an increase in oxygen mass-transfer polarization and, as a consequence, restricts oxygen transport to the cathode catalyst. This phenomenon is relevant at intermediate current densities where the methanol cross-over is still significant; whereas it is negligible at both low and high current densities. In fact, oxygen mass transport is not the rate determining step at low current densities whereas the methanol permeation is generally low at high current density due to the electrochemical methanol consumption at the anode catalyst layer.

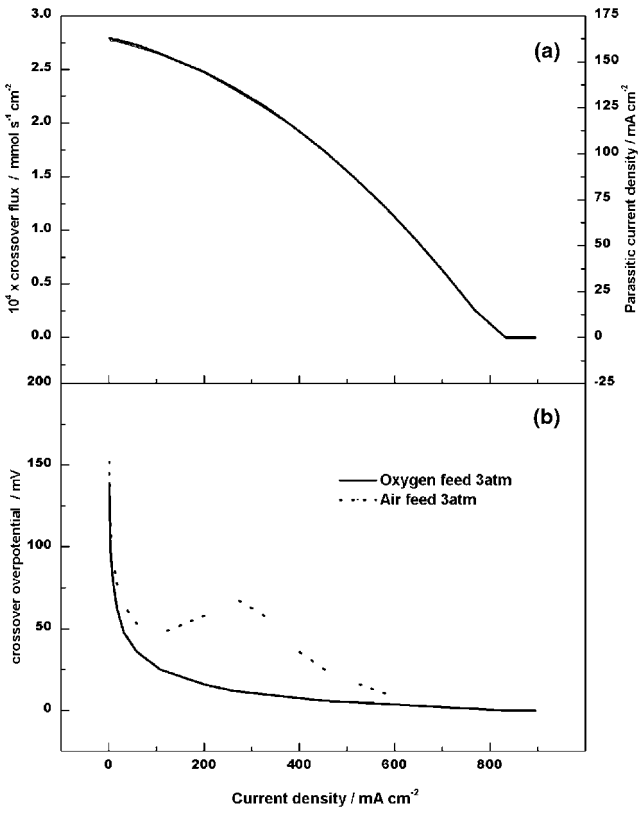

Fig. 6. (a) Computed methanol cross-over flux, and (b) the estimated cathode cross-over overpotential for the oxygen and air-fed SPE-DMFCs.

As mentioned earlier, the occurrence of a parasitic current is not the only mechanism responsible for the cathode polarization loss due to methanol cross-over. An even more relevant effect is the irreversible adsorption of methanol on the catalyst surface and its slow oxidative removal leading to a reduction in the available catalyst surface for the oxygen electrocatalysis.

An electrocatalyst for oxygen reduction can show a methanol-tolerant behaviour according to one of the following mechanisms: (i) a shift of the methanol

adsorption equilibrium to a lower value of methanol coverage for the selective catalyst, or (ii) increased CO oxidation and consequent availability of catalytic sites for oxygen reaction for the non-selective catalyst.

To evaluate the selectivity of Pt–Fe catalyst towards methanol oxidation, we simulated DMFC polarization curves with both the aforesaid assumption for selectivity where no methanol oxidation occurs at the cathode with perfect non-selectivity where entire methanol at the cathode reacts. The simulated performance data for oxygen feed and non-selective catalyst, plotted in Figure 7(a), show a better fitting to the experiment, although the difference with the selective catalyst is small owing to the high oxygen concentration. Both simulations use the same $ai_{0,\mathrm{ref}}$ value, that is the preexponential kinetic parameter proportional to the catalyst active area as shown in Equation (6). On the other hand, DMFC polarization data with air-fed cathode containing selective catalyst fit better with the experiments (Figure 7(b)). Besides, the DMFC with the selective catalyst maintains the same $ai_{0,\mathrm{ref}}$ value both for air and oxygen-fed cathodes, while the DMFC with non-selective catalyst results in an increase of $ai_{0,\mathrm{ref}}$ value while changing from oxygen to air feed at the cathode, which can be interpreted as an increase in active catalyst area. Such an unexpected increase of $ai_{0,\mathrm{ref}}$ is not easily explained from a mechanistic interpretation. The simulated performance of the selective catalyst appears to be more consistent with a mechanistic analysis of the performance, although the modeling analysis is not quite sensitive to quantitatively assess the degree of selectivity of the PtFe catalyst.

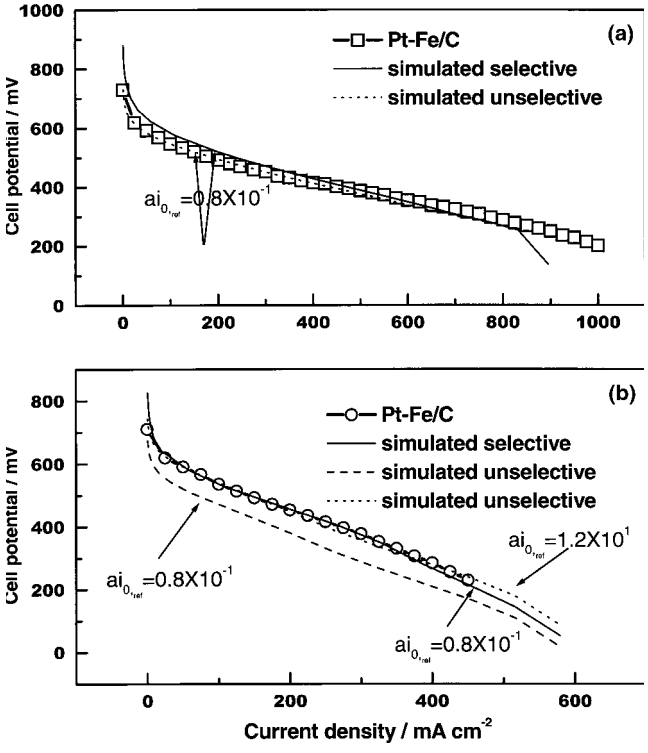

Fig. 7. Experimental and simulated performance curves both in presence and absence of the parasitic current due to methanol cross-over for (a) oxygen and (b) air-fed SPE-DMFCs.

5. Conclusions

The study clearly suggests Pt–Fe to be an effective methanol-tolerant oxygen-reduction catalyst. It has been possible to achieve a power density value as high as 250 mW cm^{-2} with oxygen and 120 mW cm^{-2} with air employing Pt–Fe/C as cathode catalyst in SPE-DMFCs. The study shows a close fit between the experimental polarization data for the SPE-DMFCs and the numerically derived polarization data. It is suggested that, unlike Pt/C, there is little change in the active-catalyst area for Pt–Fe/C due to methanol cross-over during the operation of the SPE-DMFC.

References

1. A.S. Aricò, S. Srinivasan and V. Antonucci, *Fuel Cells* **1** (2001) 1.
2. M.K. Ravikumar and A.K. Shukla, *J. Electrochem. Soc.* **143** (1996) 2601.
3. A. Heinzel and V.M. Barragán, *J. Power Sources* **84** (1999) 70.
4. P.S. Kauranen and E. Skou, *J. Electroanal. Chem.* **408** (1996) 189.
5. V. Trapp, P. Christensen and A. Hamnett, *J. Chem. Soc. Faraday Trans.* **92** (1996) 4311.
6. R.W. Reeve, P.A. Christensen, A. Hamnett, S.A. Haydock and S. C. Roy, *J. Electrochem. Soc.* **145** (1998) 3463.
7. N. Alanso-Vante, P. Bogdanoff and H. Tributsch, *J. Catal.* **190** (2000) 240.
8. M. Bron, P. Bogdanoff, S. Fiechter, I. Dorbandt, M. Hilgendorff, H. Schulenburg and H. Tributsch, *J. Electroanal. Chem.* **500** (2001) 510.
9. H. Tributsch, M. Bron, M. Hilgendorff, H. Schulenburg, I. Dorbandt, V. Eyert, P. Bogdanoff and S. Fiechter, *J. Appl. Electrochem.* **31** (2001) 739.
10. N. Alonso-Vante, B. Schubert and H. Tributsch, *Mater. Chem. Phys.* **22** (1989) 281.
11. A.K. Shukla and R.K. Raman, *Ann. Rev. Mater. Res.* **33** (2003) 155.
12. S. DurÓn, R. Rivera-Noriega, G. Poillerat and O. Solorza-Feria, *J. New Mat. Electrochem. Systems* **4** (2001) 17.
13. S. DurÓn, R. Rivera-Noriega, M.A. Leyva, P. Nkeng, G. Poillerat and O. Solorza-Feria, *J. Solid State Electrochem.* **4** (2000) 70.
14. K. Scott, A. K. Shukla, C. L. Jackson and W.R.A. Muleman, *J. Power Sources*, (in press).
15. H.G. Petrow and R.J. Allen, *US Patent* 3 992 331 (1976).
16. H.G. Petrow and R.J. Allen, *US Patent* 3 992 512 (1976).
17. H.G. Petrow and R.J. Allen, *US Patent* 4 044 193 (1975).
18. Z. Wei, H. Guo and Z. Tang, *J. Power Sources* **62** (1996) 233.
19. Du Pont™ Nafion® PFSA Membrane, NAE101, Nov. (2002).
20. S. Mukerjee and S. Srinivasan, *J. Electroanal. Chem.* **357** (1993) 201.
21. G. Murgia, A.K. Shukla, L. Pisani and K. Scott, *J. Electrochem. Soc.* **150** (2003) A1231.
22. L. Pisani, G. Murgia, M. Valentini and B. D'Aguanno, *J. Electrochem. Soc.* **149** (2002) A898.
23. D. Natarajan and T.V. Nguyen, *J. Electrochem. Soc.* **148** (2001) A1324.
24. A.K Shukla, M. Neergat, P. Bera, V. Jayaram and M.S. Hegde, *J. Electroanal. Chem.* **504** (2001) 111.
25. S. Sun, C.B. Murray, D. Weller, L. Folks and A. Moser, *Science* **287** (2000) 1989.

26. G.K. Williamson and W.H. Hall, *Acta Metall.* **1** (1953) 22.
27. A.K. Shukla, R.K. Raman, N.A. Choudhury, K. R. Priolkar, P. R. Sarode, S. Emura and R. Kumashiro, *J. Electroanal. Chem.* **563** (2004) 181.
28. H. Uchida, H. Ozuka and M. Watanabe, *Electrochim. Acta* **47** (2002) 3629.
29. T.E. Springer, T. A. Zawodzinski and S. Gottesfeld, *J. Electrochem. Soc.* **138** (1991) 2334.
30. K. Scott, W. Taama, and J. Cruickshank, *J. Power Sources* **65** (1997) 159.
31. Z. Ogumi, Z. Takehara and S. Yoshizawa, *J. Electrochem. Soc.* **131** (1984) 769.
32. D.M. Bernardi and M.W. Verbrugge, *J. Electrochem. Soc.* **139** (1992) 2477.
33. D.R. Lide and H.P.R. Frederikse, '*Handbook of Chemistry and Physics*', (CRC Press, Boca Ratton, OH, 2000).
34. X. Ren, T.A. Zawodzinski Jr., F. Uribe, H. Dai and S. Gottesfeld, *in* I, S. Gottesfeld, G. Halpert, A. Landgrebe (Eds), 'Proton Conducting Fuel Cells', PV 95-23, p. 284, The Electrochemical Society Proceeding Series, Pennington, NJ (1995).